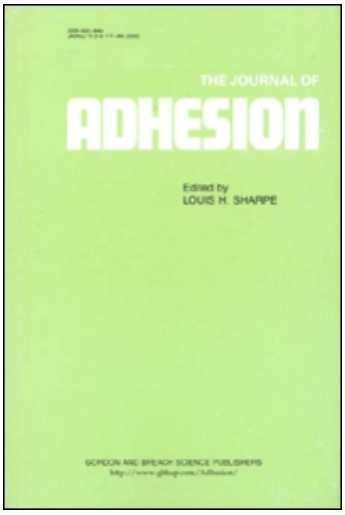

The Journal of Adhesion
Publication details, including instructions for authors and subscription information:
http://www.informaworld.com/smpp/title~content=t713453635

Interfacial Mechanisms of Moisture Degradation in Graphite-Epoxy Composites

D. H. Kaelble[a]; P. J. Dynes[a]; L. W. Crane[a]; L. Maus[b]
[a] Science Center. Rockwell International, Thousand Oaks, California, U.S.A. [b] Tulsa Division, Rockwell International, Tulsa, Oklahoma, U.S.A.

To cite this Article Kaelble, D. H. , Dynes, P. J. , Crane, L. W. and Maus, L.(1975) 'Interfacial Mechanisms of Moisture Degradation in Graphite-Epoxy Composites', The Journal of Adhesion, 7: 1, 25 — 54
To link to this Article: DOI: 10.1080/00218467508078896
URL: http://dx.doi.org/10.1080/00218467508078896

J. Adhesion, 1974, Vol. 7, pp. 25–54

Printed in Scotland

Interfacial Mechanisms of Moisture Degradation in Graphite-Epoxy Composites

D. H. KAELBLE, P. J. DYNES and L. W. CRANE

Science Center, Rockwell International, Thousand Oaks, California 91360, U.S.A.

L. MAUS

Tulsa Division, Rockwell International, Tulsa, Oklahoma, U.S.A.

(*Received April 15, 1974*)

A detailed study of the kinetics of environmental degradation in graphite–epoxy composites shows a close correlation between analytical predictions and experimentally observed changes in interlaminar shear and fracture energy response under high moisture exposure conditions. Unaged composite specimens exhibit high interlaminar shear strength $\lambda_b \geq$ 850 kg/cm^2 (12,000 psi) and relatively low fracture energy $W_b/A \simeq$ 10–20 kg cm/cm^2 (56 to 112 lb. in./in.^{2}). Exposure to 95% relative humidity or water immersion at 100°C for times $t \geq 200$ hours produces a 30 to 50% reduction in λ_b accompanied by a concurrent two to fivefold increase in W_b/A and acoustic energy absorption. These property changes are shown to be irreversible and directly related to cumulative moisture degradation of the fiber-matrix interfacial bond. The magnitudes of these property changes are consistent with surface energy analysis and micro-mechanics predictions which show that fracture energy response optimizes at intermediate values of interlaminar shear strength.

1. INTRODUCTION

This study forms part of a more general program addressed to developing a better understanding of the mechanisms of interfacial bonding and environmental stability in polymer matrix composites.[1-3] Several published studies have shown that exposure of graphite fiber reinforced epoxy or polyester composites to water immersion or water vapor at elevated temperature produces decreases in interlaminar shear strength accompanied by rising or

falling values of fracture toughness.[2, 4-6] An approach to the correction of this moisture sensitivity has been suggested by Kaelble [2, 3] based upon a modified Griffith–Irwin model for interfacial failure and a micro-mechanics model for fracture energy due to fiber debonding

The first objective of this study is to evaluate the thermodynamic and kinetic aspects of shear strength degradation in uniaxial reinforced graphite–epoxy composites exposed to high moisture and elevated temperature. The second objective is to analyze the relationships between interlaminar shear strength, fracture energy and acoustic response during environmental degradation.

2. MATERIALS AND METHODS

The graphite fiber chosen as reinforcement was Hercules HTS® which is supplied as a twist free tow containing 10,000 continuous filaments. This fiber is prepared from a polyacrylonitrile (PAN) precursor and surface

TABLE I

Surface properties of components in graphite-epoxy laminates at 23 ± 1°C

Material	$\gamma_{SV}^{d} \pm \delta^{d}$ (dyn/cm)	$\gamma_{SV}^{p} \pm \delta^{p}$ (dyn/cm)	$\gamma_{SV} \pm \delta$ (dyn/cm)
Hercules HTS® graphite fiber	25.9 ± 1.5	25.7 ± 3.3	51.6 ± 2.3
Bloomingdale BP-907® modified epoxy (cured under dry N_2)	37.2 ± 3.1	8.3 ± 2.0	45.5 ± 1.2
Hercules 3002® cyclo aliphatic epoxy (cured under dry N_2)	28.9 ± 3.2	25.0 ± 4.7	53.9 ± 2.0

treated to improve interlaminar shear strength. Two epoxy resin systems, BP-907® a modified epoxy (Bloomingdale Division of American Cyanamide) and 3002® a cycloaliphatic epoxy (Hercules) were employed as matrix materials.

Wettability measurements and surface energy analysis methods detailed in previous reports[1, 2, 7] were applied to define the dispersion γ_{SV}^{d} and polar γ_{SV}^{p} components of solid–vapor surface tension $\gamma_{SV} = \gamma_{SV}^{d} + \gamma_{SV}^{p}$ properties for both fiber and cured epoxy resin components of the reinforced composites. Surface property data for the components are summarized in Table I and relevant mechanical properties in Table II.

Curing studies of both BP907 and 3002 epoxy resin systems were conducted by differential scanning calorimetry (DSC) by methods described in previous reports.[8] Uniaxially reinforced composite plates as described by Table III were molded using the preimpregnation method. Aligned fibers are impregnated with a solution of the uncured epoxy and wound ten turns per inch on

TABLE II

Mechanical properties of components in graphite-epoxy laminates at 23 ± 1°C

Material	Shear modulus G(kg/cm^2)	Tensile modulus E(kg/cm^2)	Tensile strength σ_b(kg/cm^2)
Hercules HTS (diam. = 8.9 ± 0.4 μm)	—	$(2.53 \pm 0.28) \cdot 10^6$	$(2.46 \pm 0.35) \cdot 10^4$
BP 907 epoxy (cured)	$\simeq 1.19 \cdot 10^4$	$\simeq 3.6 \cdot 10^4$	—
3002 epoxy (cured)	$\simeq 1.19 \cdot 10^4$	$\simeq 3.16 \cdot 10^4$	—

a 9 inch diameter drum to form a single ply sheet of 30 inches width supported on a Teflon-glass release cloth. This 27 × 30 inches sheet was dried and cut to form six 13 × 9 inches plies in subsequent lamination. Normally 18 plies were laid up in uniaxial fiber arrays and cured by temperature-pressure

TABLE III

Constituents and volume fractions of components in uniaxially reinforced graphite-epoxy composite panels

Reinforced composite panel	SC1	SC2	SC3
Fiber	HTS	HTS with PVA size	HTS
Resin	BP-907	BP-907	3002
Volume fractions:			
Fiber (%)	40.3	39.8	41.0
Resin (%)	58.3	60.0	54.0
Voids (%)	1.4	0.2	5.0
Densities:			
Fiber ρ_F(gm/cc)	1.74	1.74	1.74
Matrix ρ_M(gm/cc)	1.22	1.21	1.22
Composite ρ_c(gm/cc)	1.41	1.42	1.37

staging, according to manufacturer's recommendation, to achieve final cure conditions of 177°C for 2 hours. Final dimensions of the cured panels were 13 × 9 × 0.3 inches with a fiber volume fraction $V = 0.40 \pm 0.01$.

In conjunction with the simple fiber–resin combinations indicated by Panels SC1 and SC3 of Table III and additional panel SC2 was manufactured in which the HTS graphite fiber was sized with polyvinyl alcohol PVA (1.5% of PVA based on graphite dry weight). The objective in preparing panel SC2 was to determine whether the presence of a nominally water soluble PVA polymer at the fiber–matrix interface substantially modified the kinetics of degradation in mechanical response properties as compared to Panel SC1. The presence of a relatively high void volume fraction of 5.0% in Panel SC3 was an additional variable of interest to this study of moisture degradation effects.

Measurements of interlaminar shear strengths using the standard short beam shear test produced combinations of tensile and shear failure which indicated this test was not useful in detailed study of environmental degradation effects. The sample and test geometry shown in the upper portion of Figure 1 was developed as a replacement of the short beam shear test. In the compression shear test shown in Figure 1 a sample 1.50 × 0.50 × 0.50 cm

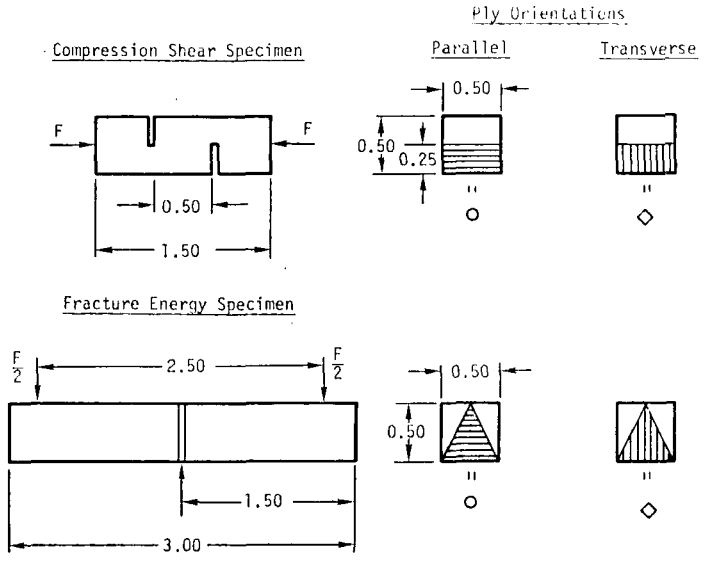

FIGURE 1 Test specimens for interlaminar shear strength (upper) and fracture energy (lower) measurement.

outer dimensions is cut from the panel with fibers parallel to the sample length. Two 0.05 cm wide by 0.25 cm deep grooves are then cut from opposite faces of the specimen to generate a shear plane of 0.50 × 0.50 cm dimensions in the center of the specimen when subject to end compression. As shown by the end views of Figure 3 these grooves can be oriented to shear

parallel or transverse to the fiber plies. The interlaminar shear strength is described by the following relation

$$\lambda_b = F_b/A_0 \tag{1}$$

where F_b = the compressional force at break and $A_0 = 0.25\ \text{cm}^2$ is the nominal cross section area of the shear plane.

Fracture energy measurements in slow crack propagation were conducted using the three point bend specimen designed by Tatersall and Tappin[9] and illustrated in the lower view of Figure 1. These specimens have outer dimensions 3.00 × 0.50 × 0.50 cm with fibers oriented parallel to the sample length. Two intersecting center grooves of 0.05 cm wide are cut in the specimen to form a center cross section in the form of an isosceles triangle of cross section area $A_0 = 0.125\ \text{cm}^2$. The geometry of flexure loading shown in Figure 1 generates a crack at the apex of the isosceles triangle section which propagates downward to the base of the triangle. The work of fracture per unit area W_b/A is defined as:

$$\frac{W_b}{A} = \frac{1}{A_0}\int_{L=0}^{L_b} F dL \tag{2}$$

where the force-displacement integral is automatically recorded by the Instron integrator accessory.

The specimen geometries shown in Figure 1 were cut using a 0.05 cm wide liquid cooled-diamond saw. In all cases the fiber axis is parallel to specimen length. The two orientations of the groove cuts relative to the fiber plies shown in Figure 1 permitted propagation of compression shear failure and crack propagation parallel (circle data points) and transverse (diamond data point) to the planes of the fiber plies.

These samples were aged for varied times using 100°C and 95% R.H. vapor phase immersion over a saturated water solution of K_2SO_4 as described by Gahimer and Nieske.[10] A second group of samples were subjected to full water immersion exposure at 100°C for varied times. Compression shear and fracture energy measurements were conducted at 23 ± 1°C immediately after the sample is withdrawn from the high moisture environment. Constant Instron cross-head speeds of 0.02 cm/min for compression shear and 0.05 cm/min for fracture energy measurement were applied. Sample weighing immediately upon removal from the high moisture environment and subsequent to extended desiccation over anhydrous calcium sulphate permits determination of moisture content at the time of fracture testing.

Subsequent to moisture exposure, fracture testing and subsequent desiccation for moisture determination, as described above, all samples were subjected to ultrasonic inspection using through transmission (C-scan) at 2.25 MHz. The samples were coupled via thin films of Nonaq grease (Fisher

Scientific Co.) to the signal transmission and detector transducers of a Sperry Reflectoscope UM721 (Customation Industries, Inc.). The sound transmission path was vertical in the cross section views shown in Figure 1 with the wave front parallel (circle data points) or transverse (diamond data points) to the ply orientations. A constant compression force of 8.1 kg between the ultrasonic transducers and the upper and lower faces of the test specimen adjacent to the fracture zone (see Figure 1) provided reproducible values of delay time $\Delta t = (t_2 - t_1)$ and signal amplitude ratio A_1/A_2 where t_1, t_2 and A_1, A_2 are the respective signal arrival times (μ sec) and amplitudes (volts) without sample (subscript 1) and with sample (subscript 2) of thickness $L = 0.50$ cm. The longitudinal sound velocity C_L(km/sec) and the acoustic absorption coefficient α_L (nepers/cm) are determined by the following standard relations:

$$C_L = L/\Delta t = L/(t_2 - t_1) \tag{3}$$

$$\alpha_L = L^{-1} \ln(A_1/A_2) \tag{4}$$

These acoustic properties reflect combined effects of moisture sorption, mechanical loading, and subsequent desiccation upon the material response.

3. INTERLAMINAR SHEAR STRENGTH DEGRADATION

a) Surface energy aspects

Previous studies by us have shown that the interfacial bond between fiber and matrix under varied conditions of environmental immersion can be expressed in terms of surface energy parameters which describe (London-*d*) dispersion $\gamma^d = \alpha^2$ and (Keesom-*p*) polar $\gamma^p = \beta^2$ contributions to liquid-vapor $\gamma_{LV} = \gamma^d_{LV} + \gamma^p_{LV}$ or solid-vapor $\gamma_{SV} = \gamma^d_{SV} + \gamma^p_{SV}$ surface tension.[7] Since these definitions include the surface tension properties of water where $\gamma^d_{LV} = 21.8$ dyn/cm, $\gamma^p_{LV} = 51.0$ dyn/cm, and $\gamma_{LV} = 72.8$ dyn/cm at 20°C, this dispersion–polar interaction model forms the basis for predictions of the degradation of bond strength when the fiber–matrix interface is transferred from air to water immersion and comes to full equilibrium with the water immersion environment.[2]

Surface energy parameters required to define this three phase model where the matrix (or adhesive) is phase 1, the environmental immersion phase (air or water) is phase 2, and the fiber (or adherend) is phase 3, are represented by the following expressions:[1, 2]

$$\gamma_1 = \gamma^d_1 + \gamma^p_1 = \alpha^2_1 + \beta^2_1 \tag{5}$$

$$\gamma_2 = \gamma^d_2 + \gamma^p_2 = \alpha^2_2 + \beta^2_2 \tag{6}$$

$$\gamma_3 = \gamma^d_3 + \gamma^p_3 = \alpha^2_3 + \beta^2_3 \tag{7}$$

The parameters $\alpha = (\gamma^d)^{\frac{1}{2}}$ and $\beta = (\gamma^p)^{\frac{1}{2}}$ are introduced for notational convenience. These six surface energy terms enter a detailed statement of the Griffith relation for critical stress σ_c for crack initiation under normal plane stress loading as defined by the following expression:[2]

$$\sigma_c\left(\frac{\pi c}{2E}\right)^{\frac{1}{2}} = \gamma_G^{\frac{1}{2}} = (R^2 - R_0^2)^{\frac{1}{2}} \tag{8}$$

where the surface energy coefficients appear in the following supplementary relations:

$$R_0^2 = 0.25[(\alpha_1 - \alpha_3)^2 + (\beta_1 - \beta_3)^2] \tag{9}$$

$$R^2 = (\alpha_2 - H)^2 + (\beta_2 - K)^2 \tag{10}$$

$$H = 0.50\,(\alpha_1 + \alpha_3) \tag{11}$$

$$K = 0.50\,(\beta_1 + \beta_3) \tag{12}$$

The application of Eq. 8 assumes that the change in immersion environment does not significantly influence the system modulus E or crack length C and that the significant variable is the reversible Griffith surface energy $\gamma_G = (R^2 - R_0^2)$.

Inspection of Eq. 9 through Eq. 12 shows that the modified Griffith expression of Eq. 8 can be conveniently represented on a graph of α versus β as shown in Figure 2. The left view of Figure 2 indicates the location of the α versus β points for the matrix and fiber surfaces of Panel SC1 (see data of Table I and Table III). The right view of Figure 2 diagrams the α versus β points for Panel SC3. The vectors R(air) and $R(H_2O)$ originate at H, K as defined by Eq. 11 and Eq. 12 and terminate at $\alpha = \beta = 0$ for air and $\alpha = 4.67$ (dyn/cm)$^{\frac{1}{2}}$ and $\beta = 7.14$ (dyn/cm)$^{\frac{1}{2}}$ for water which represent the surface tension properties of these two immersion phases. The R_0 vectors shown in Figure 2 also originate at H, K and describe a circle which encloses the region where $R \leqslant R_0$ and from Eq. 8 it is predicted that $\sigma_c = 0$.

The master functions of $\sigma_c(\pi C/2E)^{\frac{1}{2}} = \gamma_G^{\frac{1}{2}}$ versus R shown in Figure 3 show air and water immersion environments as two special cases. For panel SC-1 (left view) the prediction is that $\sigma_c(H_2O)/\sigma_c(\text{air}) = 0.46$ and panel SC-3 $\sigma_c(H_2O)/\sigma_c(\text{air}) = 0.29$ for ratio of fiber-matrix debonding for constant ($\pi C/2$E). The diagrams of Figure 2 graphically detail the surface energy arguments which predict that water will substantially reduce the interfacial bond strength in both composite SC1 and SC3. The HTS graphite fiber has highly polar surface properties with $\beta_3/\alpha_3 \simeq 1.00$ which typically result from oxidative surface treatments such as hypochlorite or nitric acid etching.[1-6] Epoxy resin systems are typically polar in surface properties with $\beta_1/\alpha_1 \simeq 0.40$ *to* 1.0[1, 2] *This combination of surface properties for both resin and fiber create a bonded interface which is hydrophilic as indicated by the short* $R(H_2O)$ vectors in Figure 2.

The consequences of bonding a less polar BP907 epoxy resin of composite

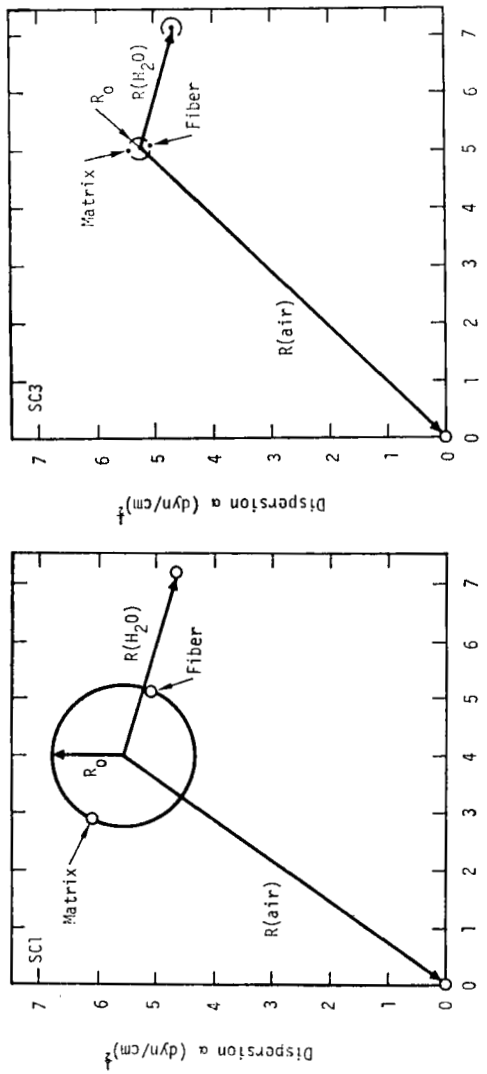

FIGURE 2 Surface energy analysis for fiber-matrix interactions for composite SC1 (left view) and composite SC3 (right view) with air and water immersion phases.

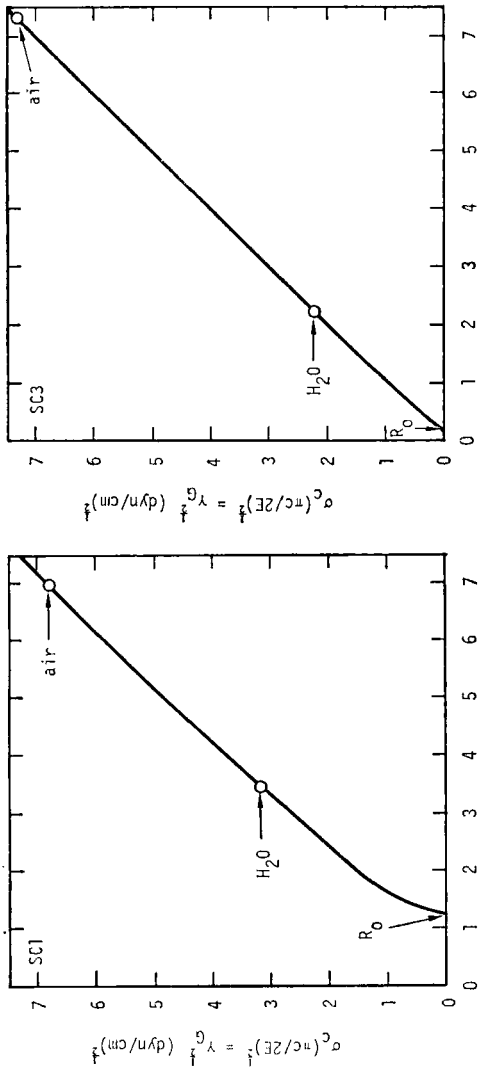

FIGURE 3 Griffith failure criteria $\sigma_c \propto \gamma_G^{\frac{1}{2}}$ for composite SC1 (left view) and composite SC3 (right view) under air and water immersion.

SC1 to the polar HTS graphite fiber are shown by both Figure 2 and Figure 3 to increase both R_0 and $R(H_2O)$ while producing a slight decrease in R(air) when compared to composite SC3. The end result as shown by the curves of Figure 3 is that water should suppress the bond strength of panel SC1 to a lesser degree than SC3.

Fracture in interlaminar shear produces shear stresses which simultaneously fracture both the fiber–matrix interface and matrix continuum between adjacent fibers. For fibers of uniform radius r_0 in regular hexagonal packing the matrix distance a separating adjacent fibers is defined by the following expression:[3]

$$a = r_0[1.074(\pi/V)^{\frac{1}{2}} - 2] \tag{13}$$

where V = fiber volume fraction. Solving Eq. 13 for $V = 0.40$ shows that $a = r_0$. Applying the geometrical model for interlaminar shear failure shown in the upper view of Figure 4, the fractional areas for interfacial f_I and matrix

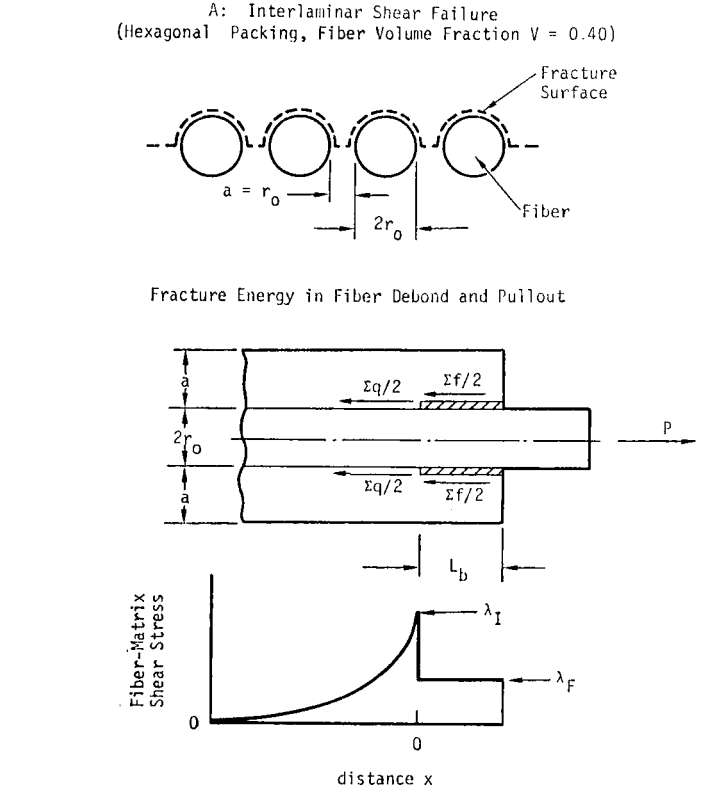

FIGURE 4 Micromechanisms of interlaminar shear failure (upper) and fracture energy measurement (lower).

f_M failure defined by the schematic of Figure 4 are given by the following relation:

$$f_I = 1 - f_M = \frac{\pi r_0}{\pi r_0 + a} = 0.76 \tag{14}$$

The composite interlaminar shear strength λ_b interfacial failure λ_I and matrix failure λ_M is obtained from the rule of mixtures:

$$\lambda_b = f_I \lambda_I + f_M \lambda_M \tag{15}$$

Consider that an unexposed laminate under air immersion displays interlaminar shear strengths

$$\lambda_{b0} = \lambda_{I0} = \lambda_{M0} \tag{16}$$

where the zero suffix represents the respective shear strengths at zero exposure time ($t = 0$) to water immersion. Under a condition of infinite ($t = \infty$) exposure time under water immersion let us further assume that:

$$\lambda_{M\infty} = \lambda_{M0} \tag{17}$$

$$\lambda_{I\infty} = \lambda_{I0} \frac{\sigma_c(H_2O)}{\sigma_c(\text{air})} \tag{18}$$

Substituting the statements of Eq. 16 through Eq. 18 into Eq. 15 we obtain the following relation:

$$\frac{\lambda_{b\infty}}{\lambda_{b0}} = (1 - f_I) + f_I \frac{\sigma_c(H_2O)}{\sigma_c(\text{air})} \tag{19}$$

For panel SC1 with $\sigma_c(H_2O)/\sigma_c(\text{air}) = 0.463$ and $f_I = 0.76$ we obtain a prediction from Eq. 19 that:

$$\frac{\lambda_{b\infty}}{\lambda_{b0}} = 0.59 \tag{20}$$

For panel SC3 with $\sigma_c(H_2O)/\sigma_c(\text{air}) = 0.298$ and $f_I = 0.76$ we obtain a prediction from Eq. 19 that:

$$\frac{\lambda_{b\infty}}{\lambda_{b0}} = 0.47 \tag{21}$$

These predictions are based upon surface energy arguments and a simplified model which translates interface degradation considerations into the composite shear failure of both interface and matrix.

b) Kinetic aspects

Previous studies have shown that a finite time is required to establish equilibrium between a composite material response and the environment to which it is exposed. A general procedure for expressing the cumulative damage effects of mechanical (M), thermal (T), or environmental (C =

chemical or corrosive) stresses is by the relation proposed by Halpin and coworkers:[11-13]

$$\phi = \exp(-Kt^b/a_T a_M a_c) \tag{22}$$

where ϕ = the cumulative degradation function, t = exposure time, K = a system constant, a_T, a_M, a_c = time shift factors relating to respective thermal, mechanical, or chemical effects, and b = a time exponent. A specialized form of Eq. 22 applicable to analysis of degradation of interlaminar shear would take the following form:

$$\phi = \frac{\lambda_b(t) - \lambda_{b0}}{\lambda_{b0} - \lambda_{b\infty}} = \exp(-t/\tau) \tag{23}$$

where it is assumed $b = 1.0$ and the relaxation time $\tau = a_T a_M a_c/K$. Rearranging Eq. 23 we obtain the following expression for the interlaminar shear strength $\lambda_b(t)$ at exposure time t by the following expression:

$$\lambda_b(t) = \lambda_{b\infty} + (\lambda_{b0} - \lambda_{b\infty}) \exp(-t/\tau) \tag{24}$$

where the relaxation time τ is defined:

$$\tau = -t/\ln \phi \tag{25}$$

One objective of the present study was to evaluate both surface energy and kinetics aspects of interlaminar shear strength degradation as outlined by the above discussion.

c) Evaluation of experimental results

The experimental curves of Figure 5 provide a graphical summary of the moisture content of composite panels SC1, SC2 and SC3 as a function of exposure time t to water vapor (95% R.H. at 100°C) and liquid water immersion at 100°C. It is evident from Figure 5 exposure times of $t \geqslant 200$ hr are required to produce maximum moisture uptake under liquid water immersion. These data also show that Panel SC3 with 5% void volume fraction (see Table 3) displays a substantially higher moisture content under liquid immersion than either SC2 or SC1. It is also evident that the polyvinyl alcohol (PVA) fiber size introduced in composite SC2 produces no substantial increase in rate or extent of moisture uptake over Panel SC1 without this water sensitive interface constituent.

Exposure to water vapour is shown by the data of Figure 5 to produce generally lower moisture content as compared to liquid water immersion. The exceptional case is the long term exposure data for Panel SC1 where the void volume fraction of 1.2% may be a factor producing equivalent effects for liquid and vapor immersion.

The effects of both water vapor (upper curves) and liquid water immersion (lower curves) on compressional interlaminar shear strength for composite

SC1, SC2 and SC3 are shown respectively in Figures 6, 7 and 8. It may be recalled from Figure 1 that the circled points represent shear parallel and diamond points traverse to the ply orientations. The experimental data of Figure 6 through Figure 8 do show a monotonic decrease from initial maximum values of $\lambda_b = \lambda_0$ to final time invariant values $\lambda_b = \lambda_\infty$ which are approached at exposure times $t \geqslant 200$ hours.

A summary of the kinetics of degradation represented by the data points

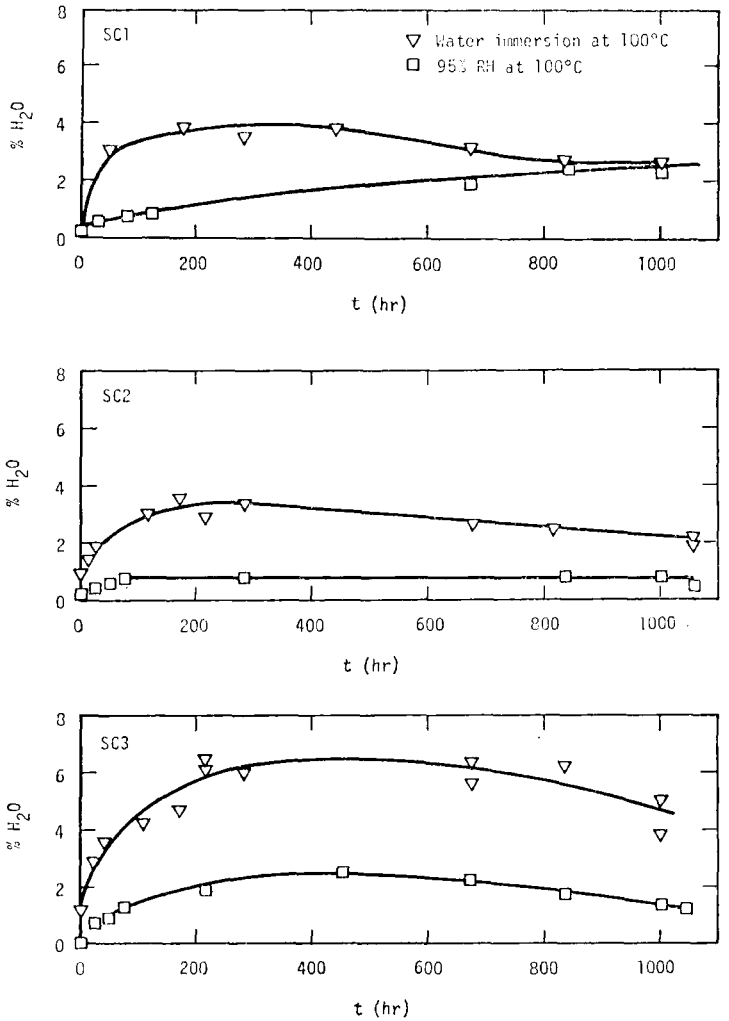

FIGURE 5 Moisture content (% by weight H_2O) versus exposure time (t) of composites SC1 (upper view) SC2 (middle view) and SC3 (lower view).

and extreme value curves of Figure 6 through Figure 8 are presented in Table 4. The magnitude and (+ or −) variability in the parameters of Table 4 represent average and extreme values required to enclose all single test data

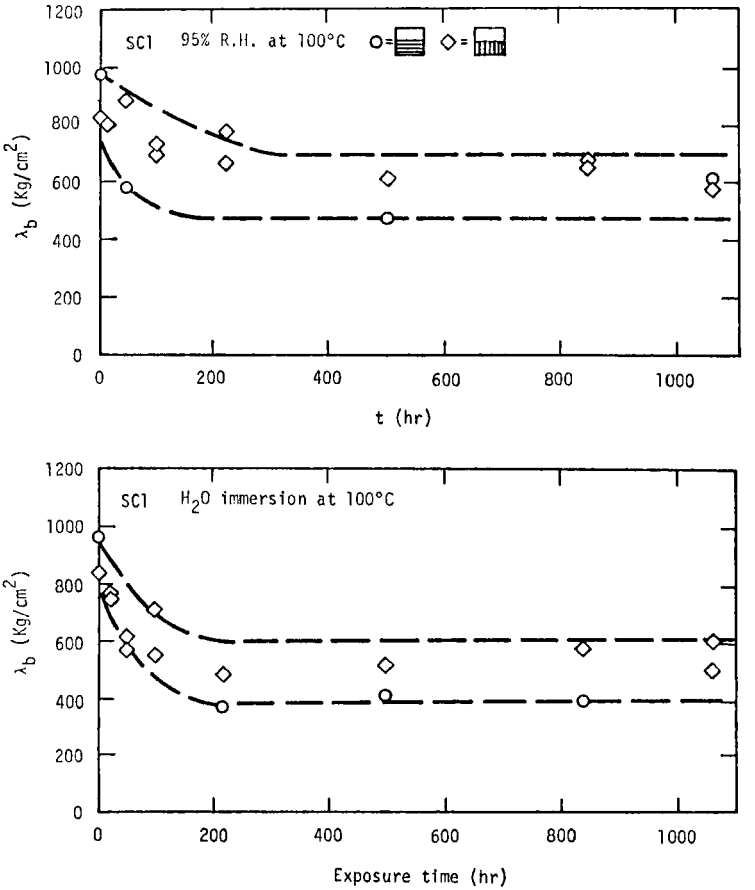

FIGURE 6 Effects of moisture exposure time t on interlaminar shear strength λ_b of composite SC1.

points of Figure 6 through Figure 8 by the functions defined by Eq. 24. The average values of $\lambda_{b0} = 825$ to 930 kg/cm^2 (11700 to 13200 psi) for unaged panels SC1, SC2 and SC3 are characteristic of strong interfacial bonding where interlaminar shear strength is characterized by cohesive failure of the epoxy matrix. The relatively high coefficients of variation ± 175 kg/cm in λ_{b0} for SC3 is reasonably attributed to the high void content (5%) for this material.

The average values of the relaxation time τ for environmental degradation appear to correlate with relatively long times required for moisture uptake as shown by the curves of Figure 5. It is evident from inspection of the data presented in Figure 4 through Figure 8 and the experimental values for

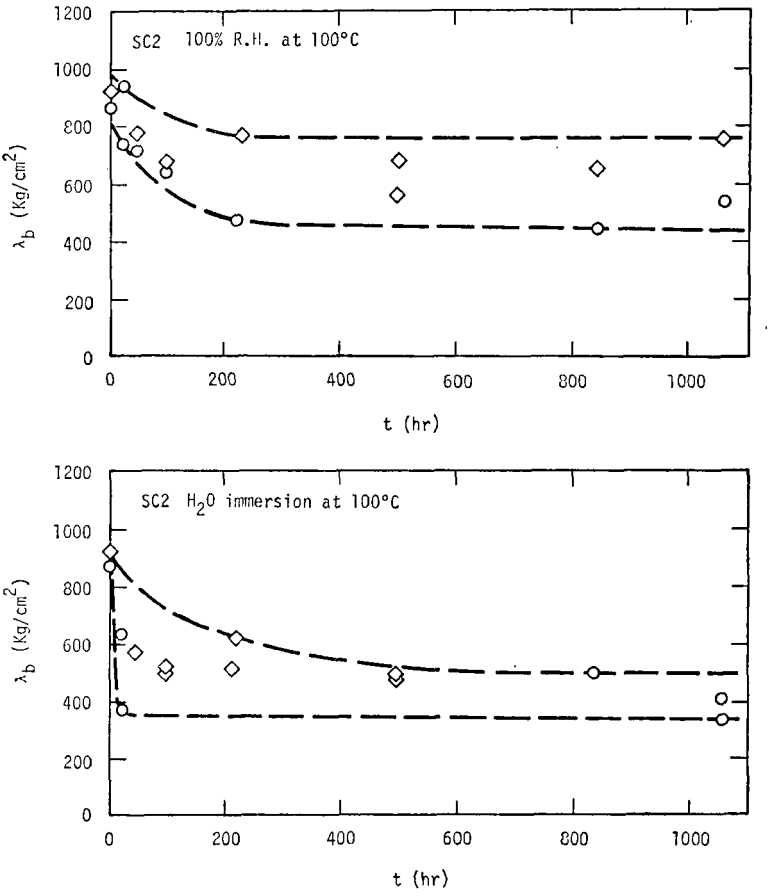

FIGURE 7 Effects of moisture exposure time t on interlaminar shear strength λ_b of composite SC2.

$\tau \simeq 60$ to 150 hours listed by Table 4 that equilibrium values for shear strength, where $\lambda_b(t) = \lambda_{b\infty}$ are established within the 1000 hours span of high moisture exposure at 100°C. The liquid H_2O immersion condition for composite panel SC1 produces an experimental value of $\lambda_{b\infty}/\lambda_{b0} = 0.56$ which compares well with the calculated value $\lambda_{b\infty}/\lambda_{b0} = 0.59$ from Eq. 19. Liquid H_2O immersed composite panel SC3 displays a somewhat lower

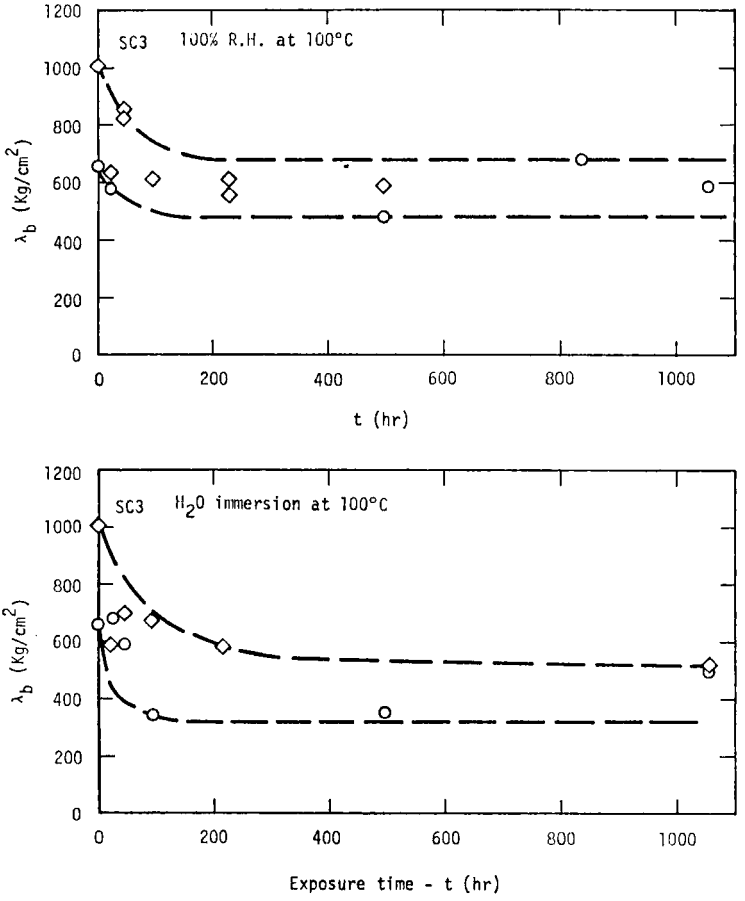

FIGURE 8 Effects of moisture exposure time t on interlaminar shear strength λ_b of composite SC3.

TABLE IV Kinetics of degradation in interlaminar shear strength
$\lambda_b(t) = \lambda_{b\infty} + (\lambda_{bo} - \lambda_{b\infty}) \exp(-t/\tau)$

Composite	Env. exp. condition	λ_{bo} (kg/cm^2)	$\lambda_{b\infty}$ (kg/cm^2)	$\lambda_{bo} - \lambda_{b\infty}$ (kg/cm^2)	τ (hour)	Average $(\lambda_{b\infty}/\lambda_{bo})$
SC1	V = vapor	875 ± 75	565 ± 115	310 ± 190	133 ± 80	0.64
	L = liquid	875 ± 75	490 ± 110	385 ± 190	61 ± 18	0.56
SC2	*V*	930 ± 70	595 ± 155	335 ± 225	64 ± 10	0.64
	L	890 ± 30	405 ± 85	485 ± 115	145 ± 110	0.45
SC3	*V*	825 ± 175	575 ± 95	350 ± 270	61 ± 14	0.69
	L	825 ± 175	420 ± 50	405 ± 225	92 ± 59	0.51

experimental ratio $\lambda_{b\infty}/\lambda_{b0} = 0.51$ which closely matches the predicted value of $\lambda_{b\infty}/\lambda_{b0} = 0.47$ from Eq. 20.

The experimental study of interlaminar shear strength degradation for composites SC1 and SC3 thus correlate very well the predictions of the surface energy and kinetic arguments. The effect of the water soluble PVA size in composite SC2 is most noticeable under liquid immersion where an extreme range of relaxation times $\tau = 145 \pm 110$ hours and a low value $\lambda_{b\infty}/\lambda_{b0} = 0.45$ represents the water degradation effect.

4. DEGRADATION EFFECTS ON FRACTURE ENERGY

a) Micro-mechanics considerations

As shown by the data of the previous section, the effect of long term exposure to either high humidity or water immersion in graphite fiber reinforced composites follows predictive relations which point out that the state of the interfacial bond depends upon the degree of equilibration to the adverse environment. Both the analysis and the experimental data point out that water exposure merely weakens rather than destroys the fiber-matrix shear bond strength. As noted in the introduction previous experimental studies have shown that water exposure with lowered interlaminar shear strength $\lambda_b(t)$ may produce both increasing or decreasing values of fracture energy W_b/A for crack propagation perpendicular to the fiber axis in uniaxially reinforced composites. This rather puzzling relationship between interlaminar shear and fracture energy behavior is clarified by a consideration of the micromechanical contributions to fracture energy in fiber reinforced composites.

A recently developed model for fracture energy is based upon the unit cell model and shear stress distribution functions schematically represented in the lower portion of Figure 4. The work of fracture W_b/A per unit area of sample cross section A is defined as the sum of the matrix shear work W_{Sb} for debonding and a frictional work W_{Fb} for fiber pull-out by the following relations:[3]

$$\frac{W_b}{A} = \frac{W_{Sb} + W_{Fb}}{A} \tag{26}$$

$$\frac{W_{Sb}}{A} = f_1(V) f_2(V) r_0 \left(\frac{E}{2G}\right)^{\frac{1}{2}} \frac{\lambda_I}{\lambda_F} \left[\frac{\sigma_b}{2} - \lambda_I \left(\frac{E}{2G}\right)^{\frac{1}{2}} f_1(V)\right] \geqslant 0 \tag{27}$$

$$\frac{W_{Fb}}{A} = \frac{f_2(V) r_0}{2\lambda_F} \left[\frac{\sigma_b}{2} - \lambda_I \left(\frac{E}{2G}\right)^{\frac{1}{2}} f(V)\right]^2 \geqslant 0 \tag{28}$$

where Table V identifies the nomenclature of the parameters of Eq. 26 through Eq. 28 and specifies values representative of the experimentally determined properties for the composite materials of this study.

The two undetermined response properties in Eq. 26 through Eq. 28 are the critical interfacial shear stress λ_I which characterizes fiber-matrix debonding and the frictional shear stress λ_F associated with fiber pull-out from the matrix. The assumptions which enter the derivations of Eq. 26 through Eq. 28 have been fully detailed in a previous report. In brief, this model

TABLE V

Physical properties of a uniaxially reinforced graphite fiber-epoxy matrix composite material

fiber radius $= r_0 = 4.45 \cdot 10^{-6}$ cm
fiber tensile strength $= \sigma_b = 2.46 \cdot 10^4$ kg/cm^2
fiber Young's modulus $= E = 2.53 \cdot 10^6$ kg/cm^2
fiber volume fraction $= V = 0.40$
matrix shear modulus $= 1.19 \cdot 10^4$ kg/cm^2
fiber packing = hexagonal (6 nearest neighbors)
volume fraction functions: $f_1(V) = 0.832, f_2(V) = 0.268, f_3(V) = 0.236$

assumes that the fracture energy element shown in the lower portion of Figure 4 is located at the apex of a crack propagation perpendicular to a uniaxial fiber array. The tensile force P acting on a fiber which traverses the crack can introduce matrix shear forces Σq and introduce a fiber-matrix debond of length L_b shown by the schematic of lower Figure 4. In the region of debond an additional set of frictional forces Σf may exist to establish a force equilibrium $P = \Sigma q + \Sigma f$. When the debond length $L = L_b$ the force $P = \pi r_0^2 \sigma_b$ and the fiber fails. If the locus of fiber failure is at $L = L_b$ the value of the frictional work W_{Fb}/A achieves the maximum value stated by Eq. 28. However, if the fiber fails outside the debond zone it follows that no pull-out occurs and $W_{Fb} = 0$. Since the locus of fiber tensile failure is statistically indeterminate the range of expected fracture energy W_b/A lies within upper and lower bounds specified by the following relation:[3]

$$\frac{W_{Sb} + W_{fb}}{A} \geqslant \frac{W_b}{A} \geqslant \frac{W_{Sb}}{A} \tag{29}$$

All parameters of Eq. 27 and Eq. 28 are specified by Table V with the exception of the shear stresses λ_I and λ_F. Information concerning the magnitude λ_I is, of course, developed by interlaminar shear strength testing as identified in Eq. 15 and subsequent relations which lead to the kinetic expression for shear strength degradation stated by Eq. 24.

The magnitude of λ_F and its dependences upon moisture degradation effects can only be estimated by indirect methods such as thermoelastic calculations based on resin shrinkage about the fiber as demonstrated by Broutman.[14] By introducing the constants of Table V into Eq. 27 and Eq. 28 we obtain the following specific relations:

$$\frac{W_{Sb}}{A}\left(\frac{\text{kg}}{\text{cm}}\right) = 1.025 \cdot 10^{-3}\,\frac{\lambda_I}{\lambda_F}(12{,}300 - 8.58\lambda_I) \tag{30}$$

$$\frac{W_{Fb}}{A}\left(\frac{\text{kg}}{\text{cm}}\right) = \frac{5.96 \cdot 10^{-5}}{\lambda_F}(12{,}300 - 8.58\lambda_I)^2 \tag{31}$$

where both λ_I and λ_F are expressed in kg/cm^2 units. The calculated functions of Figure 9 present two examples of fracture energy predictions based upon

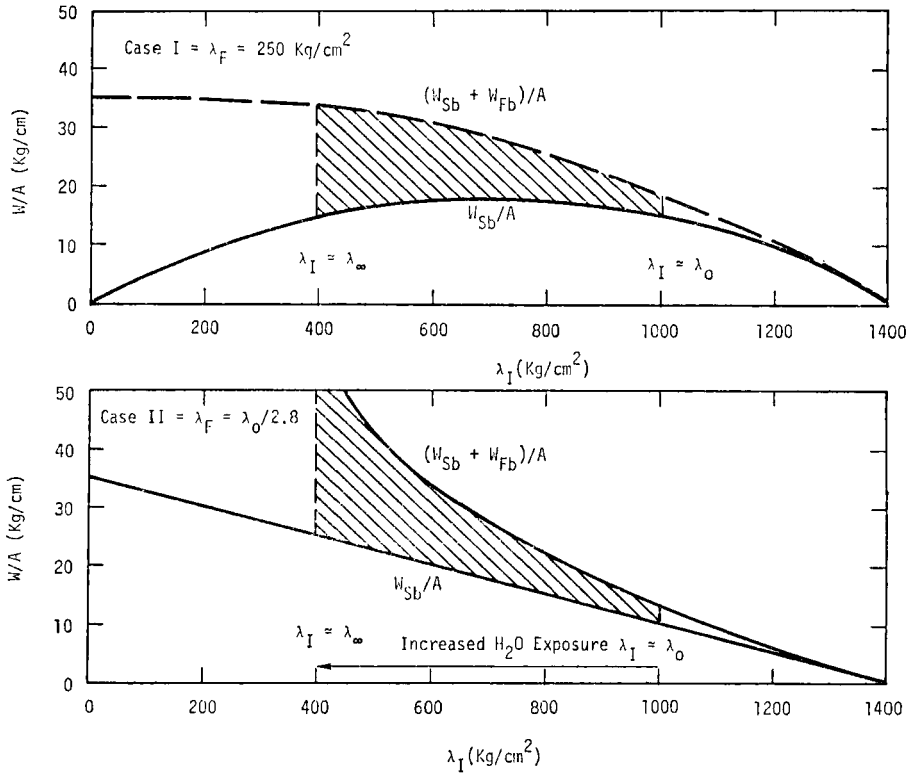

FIGURE 9 Calculated fracture energy W/A versus fiber-matrix shear bond strength λ_I based on micro-mechanics analysis.

Eq. 30 and Eq. 31. In upper Figure 9 (Case I) the magnitude of $\lambda_F = 250$ kg/cm^2 = 3450 psi is held constant while λ_I is variable from $\lambda_I = 0$ to $\lambda_I = 1415$ kg/cm^2 which characterizes fiber fracture without debonding. In the lower curves of Figure 9 (Case II) a proportionality condition $\lambda_F = \lambda_I/2.8$ is applied to represent a concurrent change in λ_F as λ_I is decreased by environmental degradation. These theoretical predictions of the dependence of W_b/A upon λ_I can be compared with measured values of W_b/A versus high moisture exposure time.

The shaded regions of Figure 9 define the upper and lower bounds for W_b/A as defined by the constraints of Eq. 29. The approximate range and variation in interfacial shear stress λ_I with moisture exposure is defined by the kinetic study of interlaminar shear degradation as summarized in Table IV.

b) Evaluation of experimental results

A graphical summary of the effects of water vapor (95% R.H. at 100°C) on the measured fracture energy W_b/A for crack propagation parallel (circles) and transverse (diamonds) to the fiber ply orientations for Panel SC1 are presented in the upper view of Figure 10. The lower view of Figure 10 shows water immersion effects at 100°C where exposure times range from

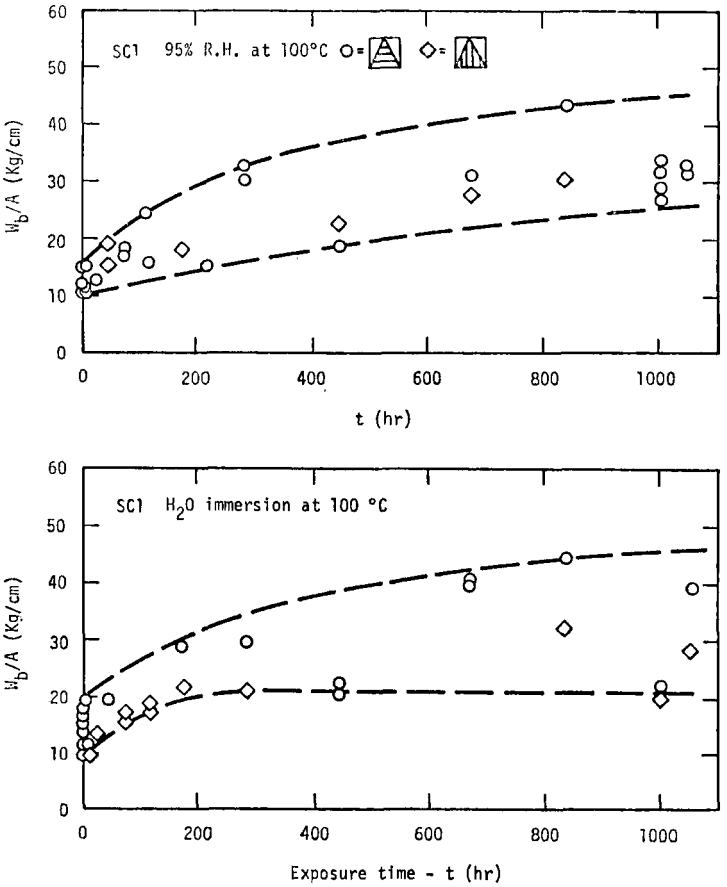

FIGURE 10 Effects of moisture exposure time t on fracture energy W_b/A of composite SC1.

$t = 0$ to 1056 hours. The dashed curves of Figure 10 represent the extreme values of the single test data points. In general the curves and data points of Figure 10 are seen to reflect the predictions presented by the shaded regions of Figure 9. As shown in Figure 10 the experimental values of W_b/A are low and display minimum scatter at $t = 0$ characteristic of high values of $\lambda_1 \simeq \lambda_M \simeq 1000$ kg/cm^2. As exposure time increases from $t = 0$ to $t = 200$ hours characteristic of the initial rapid degradation of λ_I due to water absorption the values of W_b/A increase and the scatter between maximum and minimum fracture energy increases as expected from the broadening of the shaded areas in Figure 9.

The effects of moisture exposure of panel SC2 shown in the experimental data of Figure 11 delineate enhanced scatter in fracture energy which may be

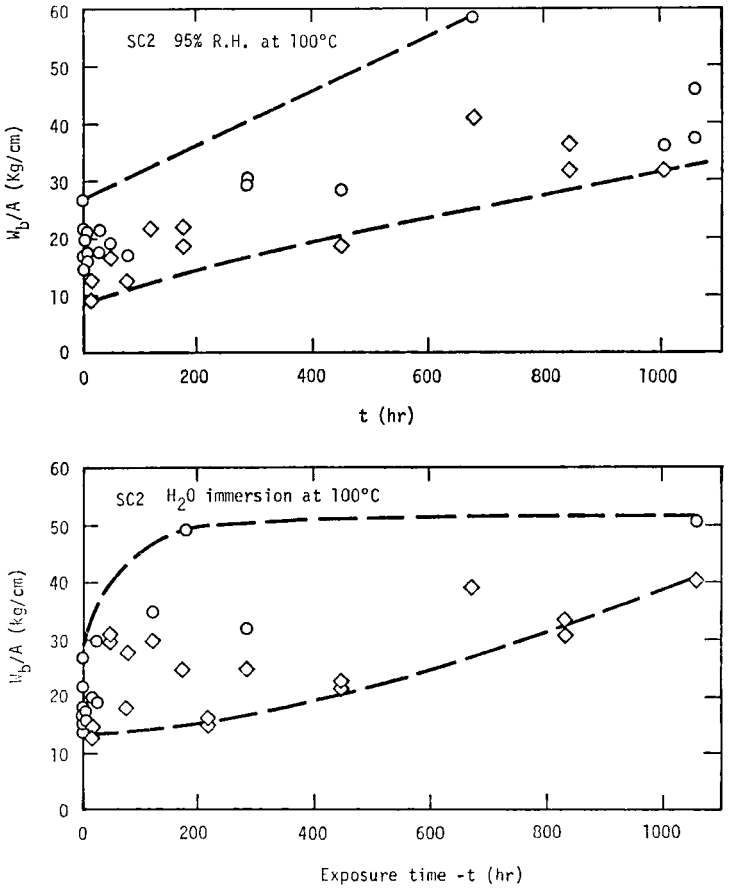

FIGURE 11 Effects of moisture exposure time t on fracture energy W_b/A of composite SC2.

attributed to the water sensitive PVA sizing present at the fiber-matrix interface of this composite. In general one finds a consistent increase in measured values of W_b/A with increasing time of moisture exposure which is consistent with degradation of λ_I and the fracture energy model summarized by Figure 9.

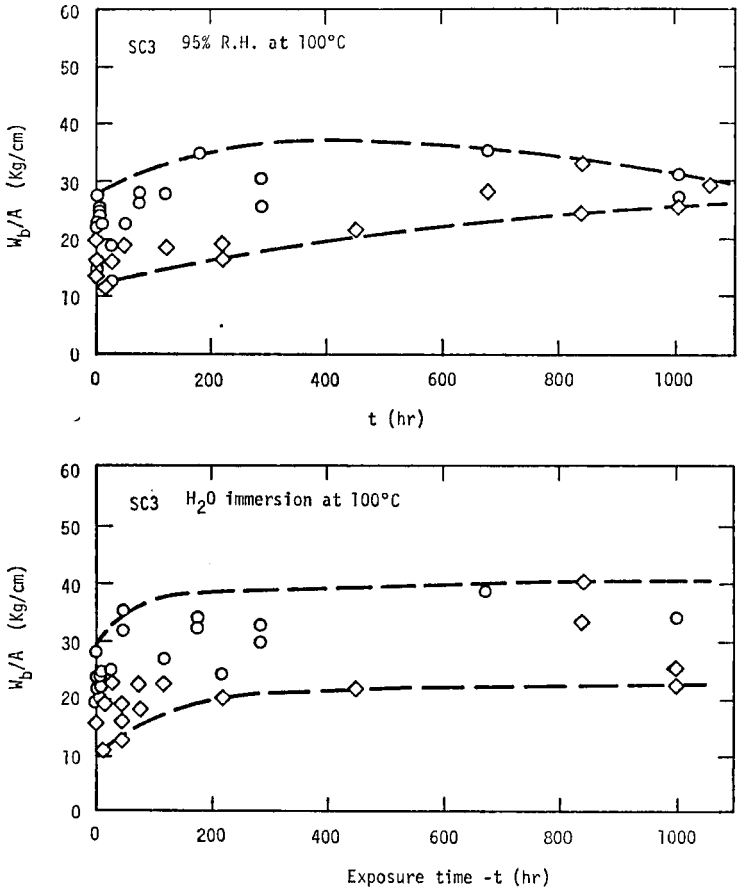

FIGURE 12 Effects of moisture exposure time t on fracture energy W_b/A of composite SC3.

The experimental values of fracture energy W_b/A and moisture degradation effects for Panel SC3 are graphically summarized in Figure 12. The large scatter in W_b/A values at $t = 0$ reflect the larger variation in λ_I due to the relatively high void content (5% voids) for Panel SC3. It may be recalled that the void structure of Panel SC3 produces a corresponding large uncertainty in interlaminar shear strength shown by λ_{b0} at $t = 0$ as shown by

the curves of Figure 8 and the data summary of Table IV. The effects of increasing exposure time on the W_b/A response of Panel SC3 follows the trends previously shown in Figure 10 and Figure 11 and predicted by the curves of Figure 9.

This experimental study of moisture degradation effects on the work of fracture correlate closely with the results predicted by the micro-mechanics model summarized by Eq. 26 through Eq. 29. In effect, the micro-mechanics model predicts that fracture energy should increase by a factor of 2 to 5 when the interlaminar shear strength which influences λ_I decreases by approximately to one-half its original value. These predictions, as graphically displayed in Figure 9, apply to a strongly bonded composite where the initial value of $\lambda_0 \simeq 1000$ kg/cm^2 and the final value of $\lambda_\infty \simeq 400$ kg/cm^2.

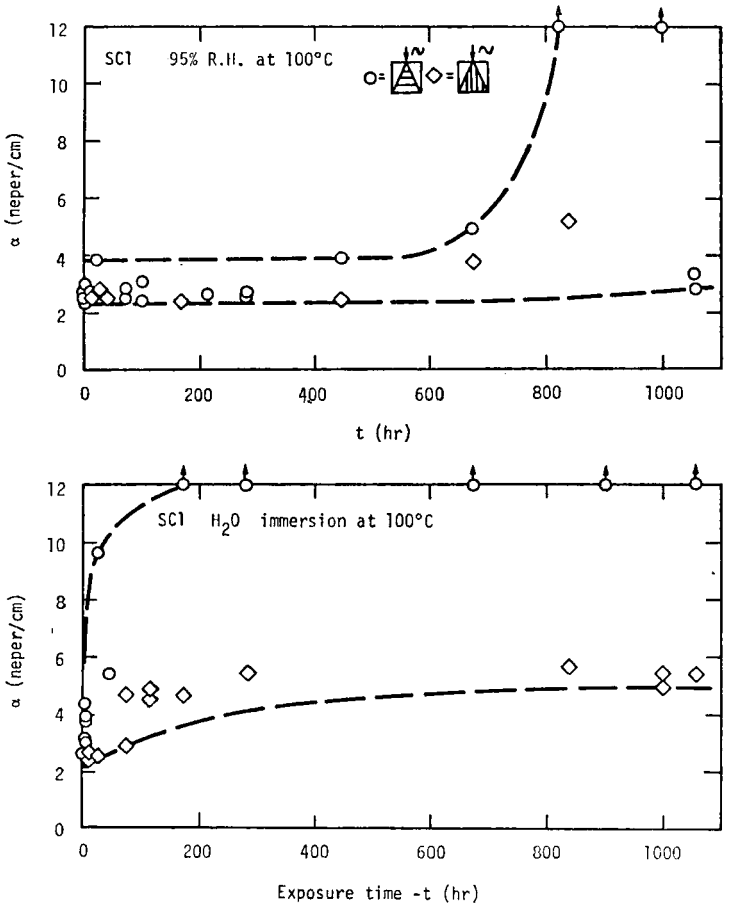

FIGURE 13 Effects of moisture exposure time t on acoustic absorption coefficient α of composite SC1.

5. DEGRADATION EFFECTS ON ACOUSTIC RESPONSE

An important aspect in studies of environmental degradation is the investigation of nondestructive test (NDT) methods which indicate the state of degradation of composite response. High frequency acoustic measurements are readily applicable to such studies and are widely utilized to detect semi-micro voids of dimensions greater than the wave length of the transmitted

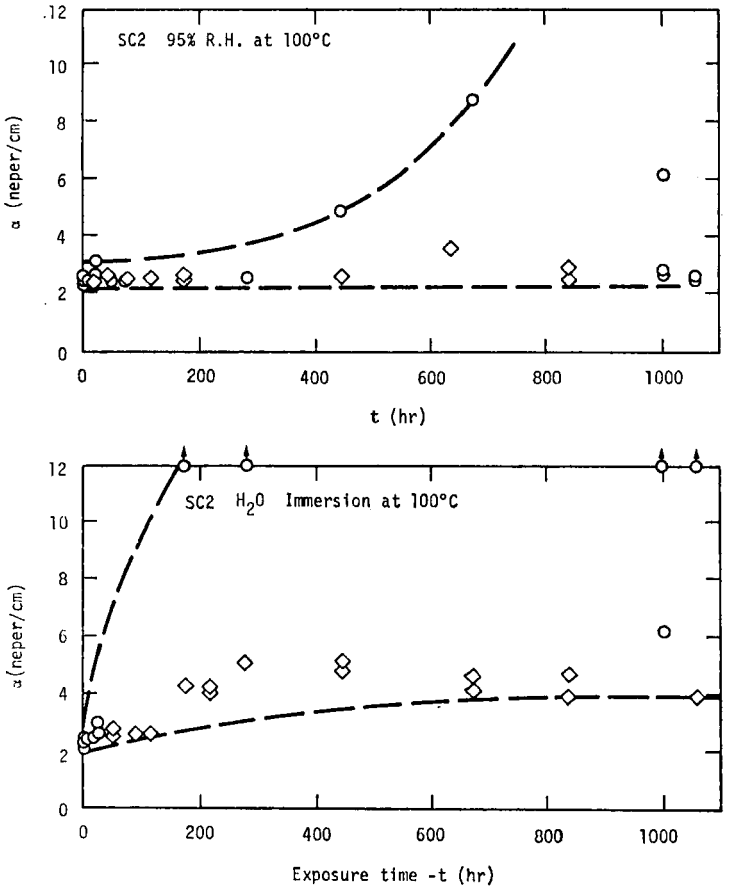

FIGURE 14 Effects of moisture exposure time t on acoustic absorption coefficient α of composite SC2.

acoustic wave in the medium under examination. The specific objective in our experiments was to determine whether sound velocity or attenuation measurements were directly sensitive to the state of the interfacial bond as evaluated by by moisture absorption, interlaminar shear strength, or fracture energy.

Sound velocity measurements on desiccated specimens subject to prior history of moisture exposure, and fracture testing for interlaminar shear or fracture energy produced averaged values of sound velocity $C_L = 3.00 \pm 0.17$ km/sec at a frequency $f = 2.25$ MHz and temperature of $23 \pm 1°C$. No significant trends were observed in the data relating to fiber ply orientation or prior moisture exposure history.

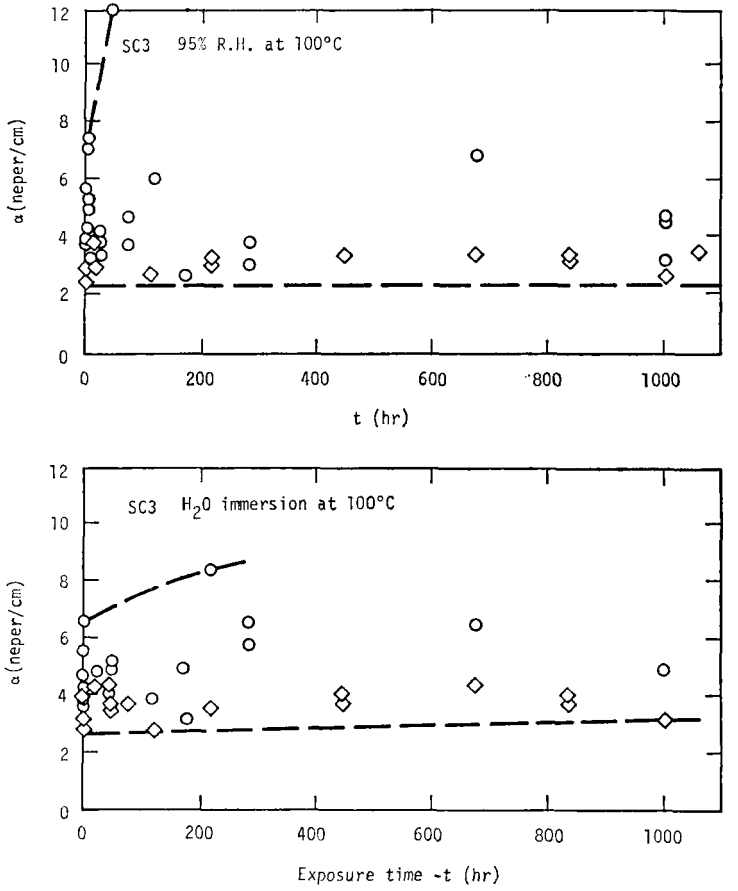

FIGURE 15 Effects of moisture exposure time t on acoustic adsorption coefficient α of composite SC3.

Acoustic attenuation response of composite specimens under equivalent test conditions were sensibly influenced by prior moisture exposure history. Measured attenuation data for sound wave fronts parallel (circles) and transverse (diamonds) to the fiber ply orientation are plotted versus moisture exposure time in the graphs of Figure 13. Inspection of Figure 13 shows that

liquid H_2O immersion at 100°C (lower view) produces a relatively large increase in acoustic adsorption coefficient α with increased exposure time compared to water vapor exposure. One also notes in the lower view of Figure 13 the circle points rise to $\alpha \geqslant 12$ neper/cm while the diamond points level at $\alpha = 5$ to 6 neper/cm at exposure times $t > 200$ hours.

The attenuation data for Panel SC2 shown in Figure 14 display moisture exposure effects which closely resemble the results of Panel SC1. Attenuation data for Panel SC3 shown in Figure 15 show a large scatter in α due to relatively high initial void content (5% voids) which appear to obscure changes due to cumulative effects of moisture exposure.

6. REVERSIBILITY OF DEGRADATION EFFECTS

The acoustic attenuation data of the previous section appear to show that prior moisture exposure effects induce permanent changes in the composite material which are not reversed by removal of the absorbed water by desiccation. This important question of reversibility of moisture degradation effects was examined in greater detail in a series of special experiments.

The general question of reversibility of moisture degradation effects is, of course, a matter of great practical interest. If full reversibility is evidenced

TABLE VI

Evaluation on interlaminar shear strength λ_{bo} and fracture energy (W_b/A_o) of unaged composite materials at 23°C

Composite material	λ_{bo} (kg/cm²)	$(W_b/A)_o$ (kg/cm)	λ_{bo}(ave) (kg/cm²)	$(W_b/A)_o$(ave) (kg/cm)
SC1	954	10.6	856 ± 76	13.5 ± 2.8
	820	10.6		
	860	12.0		
	684	13.8		
	964	18.6		
		15.6		
SC2	864	14.8	899 ± 35	19.4 ± 4.2
	918	21.4		
	854	26.4		
	920	21.4		
		17.2		
		19.8		
		14.8		
SC3	656	19.6	874 ± 165	19.0 ± 3.6
	1008	15.2		
	836	15.4		
	996	21.8		
		23.0		

the effects of prior moisture damage could be erased by simple desiccation or heat drying of the composite material and composite response would relate in a simple fashion to current moisture content. Alternatively, for nonreversible damage by moisture exposure the current moisture content would be no index of composite response and the damage induced by prior moisture exposure is permanent and nonrestorable.

The results of special tests to establish average values and standard deviations for both interlaminar shear strength λ_{b0} and fracture energy $(W_b/A)_0$ for unaged specimen of Panels SC1 through SC3 are compiled in Table VI. One notes these new values of λ_{b0} are in good agreement with the values reported in Table IV from kinetic analysis of moisture degradation. The magnitudes and standard deviations for initial fracture energy reported in Table VI are consistent with calculated predictions of Figure 9.

TABLE VII

Tests for reversibility of water vapor exposure effects on fracture energy (W_b/A)
Exposure condition: 1100 hours in 95% R.H. at 100°C
Drying condition: A = 290 hours under desiccation at 23°C
B = 1 hour under flowing dry N_2 at 200°C
C = 10 hours under flowing dry N_2 at 200°C
Test condition: Ambient atmosphere at 23°C

Drying condition	A	B	C
Composite	W_b/A (kg/cm)	W_b/A (kg/cm)	W_b/A (kg/cm)
SC1	28.2		
	31.8	26.8	28.8
	37.8	32.5	29.6
W_b/A(ave.) =	32.6	29.7	29.2
SC2			23.4
	29.9		26.8
	29.8	43.8	26.3
	33.9	19.3	21.7
W_b/A(ave.) =	31.2	31.6	24.6
SC3	35.2	27.7	
	29.8	27.8	
W_b/A(ave.) =	32.5	27.7	

In the special tests for reversibility of composite response the measurement of fracture energy was chosen as a property which increases significantly during moisture degradation and which is predicted to remain at a higher value if the damage is fully irreversible. Table VII summarizes fracture energy

measurements subsequent to long term water vapor exposure and drying under both ambient temperature desiccation and elevated temperature 200°C exposure under inert atmosphere. Table VIII presents fracture energy data where long term water immersion is followed by equivalent ambient or elevated temperature drying histories. Intercomparing the fracture energy data of Table 6 for unexposed specimens with the data of Table VII and Figure 8 for exposed and subsequently dried specimens shows that the fracture energy increases caused by interface degradation under high moisture exposure are not subsequently minimized by extended ambient desiccation.

TABLE VIII

Tests for reversibility of water immersion effects on fracture energy (W_b/A)
Exposure condition: 1100 hours water immersion at 100°C
Drying conditions: See Table VII
Test condition: Ambient atmosphere at 23°C

Drying condition	A	B	C
Composite	W_b/A (kg/cm)	W_b/A (kg/cm)	W_b/A (kg/cm)
SC1	25.4	26.9	
	30.0	24.6	
	37.1	30.3	36.0
	29.9	28.1	22.8
	W_b/A(ave.) = 30.6	27.5	29.4
SC2			24.6
	35.5	26.8	32.6
	31.6	36.9	25.4
	33.1	30.7	27.6
	W_b/A(ave.) = 33.4	31.5	27.6
SC3	47.1	34.4	
	31.0	47.6	
	W_b/A(ave.) = 36.4	41.0	

The high temperature 200°C exposure conditions of Table VII and VIII were applied to test the hypothesis that if the environmentally damaged composite is cycled above the original curing temperature of 177°C the interfacial bond may be restored. As shown in Table VII and VIII the average fracture energy for heat treated specimens is essentially equivalent to specimens dried under ambient desiccation conditions.

These results tend to support a conclusion of earlier studies [2] that moisture degradation of interfaces in graphite–epoxy composites is essentially irrever-

sible. The explanation for this finding is related to the fact that fiber-matrix bonding occurs prior to crosslinking of the epoxy matrix where local stress relaxation processes permit rheological equilibrium to be achieved at the bonded interface. Subsequent to curing the matrix remains in the cross-linked state and residual elastic stresses prevent rebonding of a damaged interface even when the resin is raised to above its glass transition temperature T_g to provide the response characteristic of a highly cross-linked elastomer.[15]

7. SUMMARY AND CONCLUSIONS

The results of this study show a close correlation between analytical predictions and experimentally observed degradation of mechanical properties in graphite–epoxy composites under high moisture aging conditions. Unaged composite specimens exhibit high interlaminar shear strength $\lambda_b \geqslant 850$ kg/cm^2 (12,000 psi) and relatively low fracture energy $W_b/A \simeq 10$–20 kg cm/cm^2 (56–112 lb. in./in.^{2}). Exposure to 95% relative humidity or water immersion at 100°C for times $t \geqslant 200$ hours produces a 30 to 50% reduction in interlaminar shear strength accompanied by a concurrent two to fivefold increase in fracture toughness and acoustic absorption properties. These property changes are shown to be irreversible and directly related to cumulative moisture degradation of the fiber-matrix interfacial bond. The magnitude of these property changes are consistent with surface energy analysis and micro-mechanics predictions which show that fracture energy response optimizes at intermediate values of shear bond strength.

The kinetic expression for cumulative moisture degradation of interlaminar shear strength (see Eq. 24) defines an environmental relaxation time τ which appears to correlate with the time scales shown for water absorption into the composite test specimens. The additional parameters of this kinetic expression define relative shear strengths at exposure times $t = \infty$ and $t = 0$ by a dimensionless ratio $\lambda_{b\infty}/\lambda_{b0}$ which are calculated from equilibrium thermodynamic arguments summarized by Eq. 19. Two technical approaches to reducing moisture sensitivity in graphite–epoxy composites are clearly identified by Eq. 24. External protective coatings which lower the diffusion rate of water into the composite material would increase τ and thereby minimize degradation for exposure times where $t \ll \tau$. The success of this approach would depend entirely upon the resistance of the coating to damage due to environmental exposure or mechanical damage.

The second approach to high moisture resistance is fundamentally stated by making $\lambda_{b\infty}/\lambda_{b0} \simeq 1.0$ and the solution involves the modification of the fiber-matrix interface such that the vectors $R(\text{air})$ and $R(H_2O)$ shown by Figure 2 display a ratio $R(\text{air})/R(H_2O) \simeq 1.0$. As discussed in previous

reports implementing this second approach requires new fiber surface treatments and selection of matrix polymers which are essentially nonpolar in both surface and bulk properties.[1, 2] A recent report by Gauchel and coworkers,[16] wherein halogenated epoxy resins are combined with surface treated S-glass fibers to form composites with remarkable moisture resistance, appears to involve this second approach.

ACKNOWLEDGEMENT

The authors acknowledge helpful discussions with Dr. G. O. Garmong. This work was supported in part by the Rockwell International IR&D Interdivisional Technology Program under the sponsorship of the Composites Technical Panel.

References

1. D. H. Kaelble, *Proc. 23rd Int. Cong. of Pure and Appl. Chem.*, vol. 8 (Butterworths London). Pp. 265–302.
2. D. H. Kaelble, P. J. Dynes and E. H. Cirlin, *J. Adhesion* **6**, 23 (1974).
3. D. H. Kaelble, *J. Adhesion* **5**, 245 (1973).
4. B. Harris, P. W. R. Beaumont and E. M. de Ferran, *J. Matl. Sci.* **6**, 238 (1971).
5. P. W. R. Beaumont and B. Harris, "The Effect of Environment on Fatigue and Crack Propagation in Carbon Fiber Reinforced Epoxy Resin," Paper 49, Proc. Int. Conf. on Carbon Fibers, The Plastics Institute, London, 1971.
6. P. W. R. Beaumont and B. Harris, *J. Comp. Matl.* **7**, 1265 (1972).
7. D. H. Kaelble, *Physical Chemistry of Adhesion* (Wiley, New York, 1971). Chap. 5.
8. D. H. Kaelble and E. H. Cirlin, *J. Poly. Sci., Part C* **35**, 79 (1971); *ibid.* **35**, 101 (1971).
9. H. G. Tattersall and G. Tappin, *J. Matl. Sci.* **1**, 296 (1966).
10. F. H. Gahimer and F. W. Nieske, *Insulation*, August, 1968, pp. 39–44.
11. J. C. Halpin and H. W. Polley, *J. Comp. Matls.* **1**, 64 (1967).
12. J. C. Halpin, J. R. Kopf and W. Goldberg, *ibid.* **4**, 462 (1970).
13. J. C. Halpin, *ibid.* **6**, 208 (1972).
14. L. J. Broutman, *J. Adhesion* **2**, 147 (1970).
15. D. H. Kaelble, *J. Appl. Poly. Sci.* **9**, 1213 (1965).
16. J. V. Gauchel, J. R. Griffith, I. Steg and J. E. Cowling, "Epoxy Resins for High Performance Marine Applications," *ACS Polymer Preprints* **14** (2), 1148 (August 1973).